Featured in Physics

Circular Dichroism in Resonant Photoelectron Diffraction as a Direct Probe of Sublattice Magnetization in Altermagnets

Peter Krüger
Graduate School of Engineering and Molecular Chirality Research Center, Chiba University, Chiba 263-8522, Japan

(Received 11 April 2025; accepted 5 September 2025; published 6 November 2025)

Altermagnets are a new class of magnetic materials that are promising for spintronics technology. Here, it is shown that in altermagnets, the circular dichroism (CD) in resonant photoelectron diffraction (RPED) contains a time-reversal odd signal, which provides a direct probe of the sublattice magnetization. RPED calculations are performed for MnTe at the Mn $L_{2,3}$-edge resonance, using a combination of atomic multiplet and multiple scattering theory. A large magnetic CD is found for light helicity parallel to the Néel vector. This signal has the same angular distribution as the difference between the structural RPED of the two magnetic sublattices and its amplitude is approximately proportional to the x-ray magnetic CD in absorption of a single sublattice, thus providing a direct probe of the local magnetic moments.

DOI: 10.1103/pl1p-v5rs

Altermagnets (AMs) are a new class of magnetic materials [1–3] with great potential for spintronics applications because, among other reasons, AMs combine the possibility of spin-dependent currents [4] with fast magnetic switching [5,6]. An AM has a compensated spin structure with two equivalent magnetic sublattices of opposite spin. In this respect, AMs are a special class of antiferromagnets. In a conventional antiferromagnet, the two sublattices are connected by an inversion or a translation symmetry operation. All band states are spin-degenerate and so the carriers cannot be spin-polarized. In AMs, the two sublattices are connected by a different symmetry operation, such as a rotation or a screw axis [3]. As a consequence, spin splitting of certain band states occurs [7] and spin-polarized transport may become possible. While the knowledge of the space group of a candidate material is sufficient for deciding whether an altermagnetic phase may exist in principle, the experimental proof of the altermagnetic state is difficult. Even for ruthenium dioxide, one of the first and most studied AM candidate materials, the existence of the altermagnetic phase is still controversial [2,8]. There is a need for experiments that can reliably determine the microscopic magnetic structure of AM candidate materials. Neutron scattering is bulk sensitive and cannot be used for heterostructures and thin films, which are particularly important for device applications. X-ray magnetic circular dichroism (XMCD), on the other hand, can be used for a wide range of systems, including molecules, nanomaterials, and surfaces. It is element-selective and the local spin and orbital moment of the magnetic atoms can be directly inferred from experimental spectra via the XMCD sum rules [9,10]. The XMCD produced by a single magnetic atom is largest when the helicity vector $\mathbf{q}$ of the light is parallel to the magnetic moment. In an altermagnet with Néel vector $\mathbf{L}$, the magnetic atoms on site A (B) have a local moment per atomic volume of $\mathbf{L}$ ($-\mathbf{L}$). As there are as many A sites as B sites, the total parallel XMCD exactly vanishes. Perpendicular XMCD, on the other hand, may be nonzero in AMs. Indeed, in MnTe with $\mathbf{L} \sim [1\bar{1}00]$ and with light incoming along the crystal [0001] axis, a small net XMCD signal was observed by Hariki *et al.* [11]. This perpendicular XMCD effect is, however, by over one order of magnitude weaker than the parallel XMCD of a single sublattice and it is unrelated to the magnetic dipole moments. Moreover, it was shown that if $\mathbf{L}$ were oriented along $[11\bar{2}0]$ in MnTe, then the perpendicular XMCD would vanish by symmetry [11]. This suggests that perpendicular XMCD is not a generally applicable technique for identifying altermagnetism in candidate materials. A weak parallel XMCD signal has been predicted theoretically for the altermagnet candidates RuO_2 [12,13] and NiF_2 [14]. This parallel XMCD is either due to weak ferromagnetism [14], or to the anisotropy of the magnetic dipole operator [12,13]. In both cases, it is not directly related to the macroscopic staggered magnetisation, which is the main order parameter of compensated magnets, and which can be measured with the present method.

In this Letter, we show theoretically, that resonant photoelectron diffraction (RPED) effectively combines the magnetic information of XMCD with local structural information from photoelectron diffraction (PED) which, in the case of AMs, makes it possible to directly probe the local magnetic moments. X-ray PED is a technique for element- and site-resolved structural characterization at crystalline surfaces [15]. In RPED from valence states excited at a core-valence resonance, the structural information from PED is augmented with local electronic information from both occupied and unoccupied valence states. Thereby, valence band photoemission data can be decomposed into contributions from different atomic sites near the surface [16]. Morscher *et al.* [17] showed that for a ferromagnetic surface, the magnetization direction can be inferred from the circular dichroism (CD) signal in RPED, which is a direct consequence of the XMCD in the x-ray absorption step of the resonant photoemission (RPES) process [18]. However, CD also occurs in RPED from nonmagnetic systems [19]. Such CD in angular distribution is a photoemission final state effect due to scattered wave interference, first observed in core-level PED by Daimon *et al.* [20]. Let us note that spin-resolved RPES was suggested as a probe for local magnetic moments in antiferromagnetic and magnetically disordered systems [21] but the interpretation is controversial [22,23].

Here, we report valence-band RPES and RPED calculations from a MnTe(0001) surface with photon energies around the Mn-$L_{2,3}$ absorption edges. We find that the RPED patterns display a large magnetic circular dichroism (MCD) in parallel geometry. The photon energy dependence of the MCD is approximately proportional to the XMCD of a single magnetic sublattice and thus provides a direct measure of the local magnetic moments. The effects found here for MnTe are general for AM materials, establishing CD-RPED as a novel, powerful technique for the magnetic characterization of AM surfaces and thin films.

The crystal structure of α-MnTe is shown in Fig. 1(a). The unit cell contains two Mn sites denoted A and B, which are equivalent by a 6_3 screw axis. In the altermagnetic ground state, the Néel vector $\mathbf{L}$ is along $[1\bar{1}00]$, which is taken as the x axis. In the RPED calculations we consider a Te-terminated MnTe(0001) surface. There are two possibilities for the subsurface layer, Mn-A and Mn-B. Since a real surface unavoidably contains steps, we average all results over these two cases. We note that details of the MnTe(0001) surface structure are not fully known and may depend on sample preparation. However, the conclusions of this work are independent of the surface structure. Indeed, the main finding, namely the existence of a large MCD in the RPED pattern, is a bulk phenomenon as is evident from symmetry considerations and as we have checked by RPED simulations for bulk MnTe; see Supplemental Material (SM) [24].

The RPED calculations are done with our recent method [18], which combines crystal field multiplet theory [28] for the resonant photoemission process and real space multiple scattering theory for the propagation of the photoelectron wave [15,29]. For the latter, finite clusters with 479 atoms are used; see Fig. 1(b). For given photon energy and light helicity, a RPED calculation is performed for each of the 210 final state multiplets of the Mn($3d^4$) configuration, with the photoelectron source wave obtained from the multiplet calculation, and the RPED intensities are summed. Further theoretical and numerical details are given in SM [24].

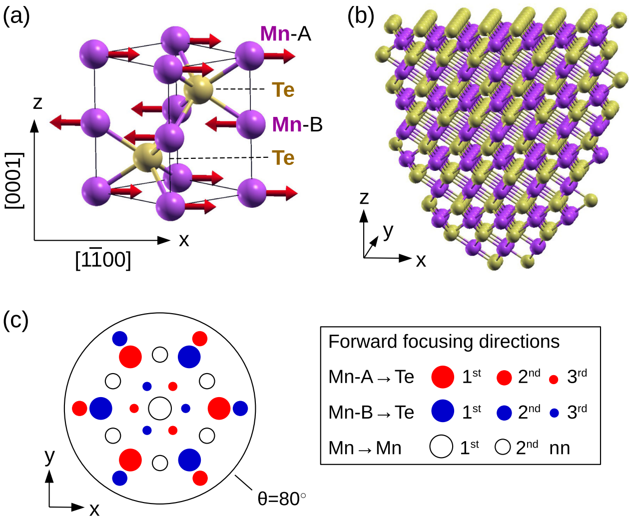

FIG. 1. (a) Ball-and-stick model of MnTe in altermagnetic ground state with Néel vector $\mathbf{L} \sim x$. (b) Cluster model of Te/Mn-A terminated (0001) surface. (c) Mayor forward focusing directions in stereographic projection. Here and in all other figures the maximum polar angle is $\theta = 80°$.

Figures 2(a) and 2(b) shows the x-ray absorption spectroscopy (XAS) and XMCD spectra obtained with the crystal field multiplet model. XAS (XMCD) is the sum (difference) spectra of light with positive (+) and negative helicity (−). In Fig. 2(a), for parallel geometry with $\mathbf{q} \sim x$, XMCD(A) and XMCD(B) are the local signals from single sites Mn-A and Mn-B, respectively. The XMCD is large and has a line shape typically for a high-spin Mn^{2+} ion [11]. XMCD(B) is exactly the negative of XMCD(A), so the total XMCD vanishes. In perpendicular geometry with $\mathbf{q} \sim z$ [Fig. 2(b)], there is a very small XMCD signal (note the scaling factor ×50) with fast oscillations. This signal is

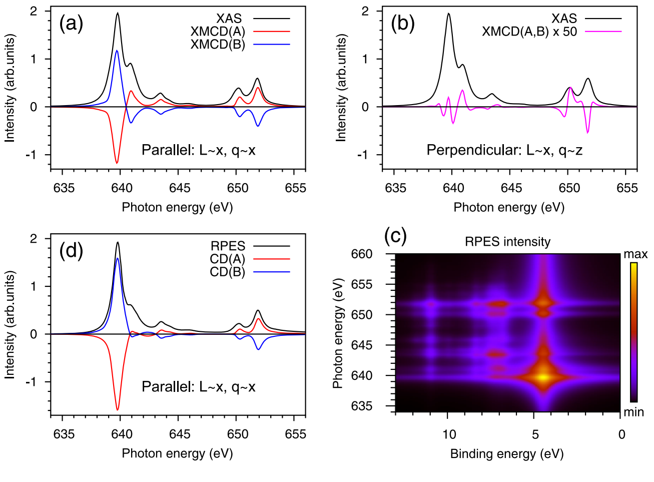

FIG. 2. Multiplet calculation for MnTe. (a) Mn $L_{2,3}$-edge XAS and XMCD spectra in parallel geometry, i.e., light helicity $\mathbf{q} \| \mathbf{L} \sim x = [1\bar{1}00]$. XMCD(S) is the atomic XMCD for site S=A,B. (b) XAS and XMCD in perpendicular geometry with $\mathbf{q} \sim z = [0001]$. The XMCD signal is multiplied by a factor of 50. (c) Resonant photoemission spectra (RPES) in parallel geometry as a 3D color plot. The color scale is linear in $\log(1 + 100 \times I)$, where I is the RPES intensity. (d) Total, binding energy integrated RPES intensity and its CD.

the same for sublattices A and B, leading to a nonzero total XMCD. The spectra in Figs. 2(a) and 2(b) agree very well with Ref. [11], validating the present crystal field multiplet model.

The RPES spectra for $\mathbf{L}, \mathbf{q} \sim x$, are plotted in Fig. 2(c) as a function of photon and binding energy with a logarithmic color scale for the intensity. There is a strong resonance at the absorption L_3-edge and a weaker one at the L_2-edge. The photoemission line shape depends rather weakly on the photon energy, although high binding energy features (e.g., the peak at 11 eV) become stronger for higher photon energy. This reflects the fact that for intermediate states above the L_3 absorption threshold, many-body “shake-up” excitations become possible that shift spectral weight from low to high binding energy.

The total RPES intensity, integrated over binding energy, is shown in Fig. 2(d). CD(A) and CD(B) are the RPES-CD spectra for sites A and B, respectively. The CD(A) line shape is very similar to XMCD(A) in Fig. 2(a) and the normalized RPES-CD is approximately equal to the normalized XMCD, i.e.,

$$I_{\mathrm{CD(A)}}(\omega)/I_{\mathrm{RPES}}(\omega) \approx I_{\mathrm{XMCD(A)}}(\omega)/I_{\mathrm{XAS}}(\omega), \qquad (1)$$

where ω is the photon energy and I is the intensity. The small differences between the line shapes in Figs. 2(a) and 2(d) are attributed to the dependence of the Auger decay probability on the intermediate multiplet state ($2p^5 3d^6$). Importantly, however, the CD in RPES displays the same sign changes as XMCD when going from site A to B or from the L_3-edge at ~640 eV to the L_2-edge at ~652 eV. This means that the local CD-RPES signal for site A or B, contains essentially the same magnetic information as the local XMCD. In XMCD and angle-integrated RPES experiments, such site-resolved information is not accessible, since the signals of A and B are of opposite sign and cancel out. However, site resolution can be achieved in an RPED experiment because the PED patterns for Mn-A emission and Mn-B emission are different. For MnTe, this will be shown numerically below and may be anticipated from the forward focusing directions in Fig. 1(c). Importantly, this argument is valid for all altermagnets, because the rotation part (in MnTe, rotation by π around z) of the space group operation between the two magnetic sublattices (in MnTe, screw axis 6_3) cannot be a symmetry operation of the point group of the magnetic sites (in MnTe, S_6) [3]. Put more simply, the two magnetic sites A and B have differently oriented crystal environments and so their diffraction patterns are distinct.

For all RPED results shown in this Letter, the photoemission intensity has been integrated over the whole valence band. The binding energy dependence of RPED contains information about the wave function character of the valence states [16,18] but this will not be discussed here. RPED patterns for a photon energy of 639.7 eV, at the maximum L_3 resonance, are shown in Figs. 3(a)–3(d), for

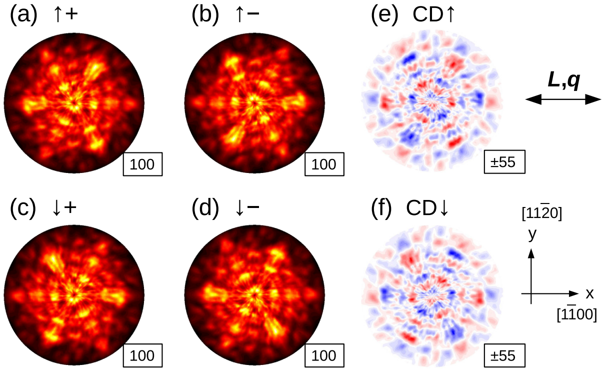

FIG. 3. Calculated resonant photoelectron diffraction patterns of MnTe(0001) at the Mn-L_3 resonance ($\hbar\omega = 639.7$ eV). Light is incoming along $[1\bar{1}00]$ with positive (+) or negative (−) helicity, as indicated. Two altermagnetic domains are considered with Néel vector $\mathbf{L}$ parallel (↑) or antiparallel (↓) to $[1\bar{1}00]$. All plots are a stereographic projections for polar angles up to 80°. In (a)–(d) the maximum intensity is yellow and minimum is black. In the CD patterns (e),(f) positive (negative) values are red (blue). The small boxes indicate the maximum intensity relative to that of (a), which is put to 100.

parallel geometry with $\mathbf{q}$ and $\mathbf{L}$ parallel to $[1\bar{1}00]$ and both signs of $\mathbf{L}$ (↑, ↓) and $\mathbf{q}$ (±). All patterns have approximate threefold symmetry. Considering the hexagonal space group of MnTe ($P6_3/mmc$) one might expect a diffraction pattern with sixfold symmetry. When the four patterns in Figs. 3(a)–3(d) are added up, i.e., light helicity and magnetization directions are averaged, then the resulting pattern has indeed sixfold symmetry; see SM [24].

The finding that the individual patterns in Figs. 3(a)–3(d) are three-fold can be understood as follows. From Fig. 2(d) we know that at the L_3-resonance, there is a large negative (positive) CD in RPES for emission from Mn-A (Mn-B). As a consequence, for (↑+), i.e., $\mathbf{L} \sim +x$ and positive helicity, the RPES intensity is much larger for Mn-B than Mn-A, and thus (↑+) looks essentially like a PED pattern from site Mn-B. Indeed, the strongest peaks in (↑+) are found at the first nearest neighbor (nn) forward focusing directions Mn-B → Te, as seen by comparison with Fig. 1(c). When reversing the light helicity, we obtain pattern (↑−) in Fig. 3(b), which is the π-rotated image of (↑+). In (↑−), emission from Mn-A sites dominates. When reversing both light helicity and Néel vector we obtain the pattern (↓−), which is a mirror image of (↑+) with regard to the x axis in the plot, i.e., with regard to the $(11\bar{2}0)$ plane. The patterns (↑+) and (↓−) are quite similar. This is expected because the relative orientation of light helicity and Néel vector is the same and so the atomic XMCD effect on each site is unchanged. We conclude that in RPED with circular polarized light, the relative orientation of helicity and Néel vector determines the Mn sublattice from which the majority of photoelectrons are emitted. When taking the difference of (↑+) and (↑−) the pattern CD↑ in Fig. 3(e) is obtained.

The CD is large, with a maximum contrast of ±55%. Upon reversal of **L** [CD↓, Fig. 3(f)] most features change sign, which shows that the CD is mostly a magnetic effect.

However, since in angle-resolved photoemission, CD is common even at nonmagnetic surfaces, it is necessary to disentangle the structural and the magnetic CD. The structural CD can be obtained by summing the patterns CD↑ and CD↓. This corresponds to a demagnetized sample with randomly oriented domains. Here, the structural CD is clearly nonzero [24]. When the patterns CD↑ and CD↓ are subtracted, any structural CD cancels, and we obtain the purely magnetic CD, given by

$$\mathrm{MCD} = I(\uparrow +) - I(\uparrow -) - I(\downarrow +) + I(\downarrow -), \qquad (2)$$

where I denotes the RPED intensity. Upon time reversal, $\mathbf{L} \to -\mathbf{L}$, or $(\uparrow) \to (\downarrow)$ in our notation, MCD changes sign, i.e., MCD is time-reversal ($\mathcal{T}$) odd. This implies that in a $\mathcal{T}$-even system, including paramagnets and conventional antiferromagnets, MCD vanishes exactly. A nonzero MCD signal is a direct signature of $\mathcal{T}$ symmetry breaking and thus provides an easy way to distinguish between altermagnets and conventional antiferromagnets. To check this point explicitly in an example, we calculated CD-RPED for the conventional antiferromagnet MnO, and found MCD = 0, as expected [24].

Note that by changing the signs of both helicity and Néel vector four independent, "fundamental" signals can be formed by linear combination. Apart from the structural CD and the MCD [Eq. (2)], we define a "structural RPED" (sum of all four patterns) and a "magnetic RPED" [24].

The MCD pattern shown in Fig. 4(a) is clearly nonzero, proving that $\mathcal{T}$ symmetry is broken in MnTe. The MCD pattern has the full S_6 point symmetry of the Mn sites. The symmetry of the pattern is not lowered by **L** or **q**, although these vectors are oriented along the nonsymmetry axis x. We have also computed the RPED-CD by assuming **L** and **q** be oriented along the z axis [24]. Remarkably, the MCD pattern is exactly the same as that in Fig. 4(a). This shows that the MCD in parallel geometry is independent of the absolute orientation of the Néel vector **L** but only depends on the *relative* orientation between **L** and helicity **q** in form of the scalar product $\mathbf{L}.\mathbf{q}$. This corroborates the conclusion that the MCD in RPED is a direct consequence of the XMCD on each ferromagnetically ordered sublattice. Indeed, XMCD in a ferromagnet also depends only on the scalar product between the magnetization **M** and **q** rather than on the absolute orientation of **M**.

Figure 4(e) shows the MCD in RPED obtained at the maximum L_2 resonance (651.8 eV). The pattern has the same symmetry as that at the L_3 resonance [Fig. 4(a)] but the intensity distribution is quite different. This is because the angular distribution of the RPES source waves strongly depends on the total angular momentum j of the $2p$-core hole in the intermediate state. For both the L_3 and the L_2 MCD pattern, the main peaks appear at forward focusing directions [see Fig. 1(c)], but the sign of the CD is reversed between L_3 and L_2. So the MCD signal in RPED changes sign in the same way as the sublattice XMCD [Fig. 2(a)] when going from the L_3-edge to the L_2-edge.

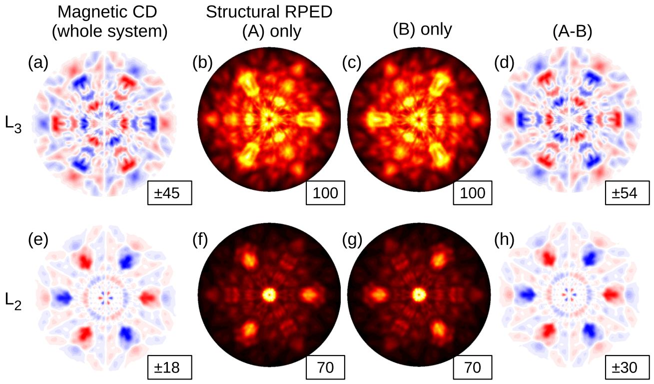

FIG. 4. Calculated RPED patterns of MnTe for circular polarized light with helicity $\mathbf{q} \| \mathbf{L} \sim [1\bar{1}00]$ at the L_3 resonance [$\hbar\omega = 639.7$ eV, (a)–(d)] or the L_2 resonance [$\hbar\omega = 651.8$ eV, (e)–(h)]. (a) Magnetic CD pattern, i.e., the difference between CD↑ and CD↓ in Figs. 3(e) and 3(f). (b) Structural RPED for sublattice Mn-A, defined as the sum of patterns (↑+), (↑−), (↓+), and (↓−), but restricted to emission from sites Mn-A. (c) Same as (b) but for sublattice Mn-B. (d) Difference between (b) and (c). (e)–(h) Corresponding patterns for the L_2 resonance. The color scale is always from minimum to maximum. The maximum intensity is indicated in the small boxes, relative to that of (b), which is put to 100.

To better understand the angular distribution of the MCD pattern, we have computed "structural RPED" patterns, defined as $(\uparrow +) + (\uparrow -) + (\downarrow +) + (\downarrow -)$, but restricted to emission from one sublattice (Mn-A or Mn-B). These patterns [Figs. 4(b), 4(c), 4(f), and 4(g)] reflect the crystal structure around a site Mn-A or Mn-B, and they are dominated by forward focusing peaks as expected from Fig. 1(c). Since the Néel vector is averaged over opposite directions, these patterns contain no magnetic information. The difference between the patterns in Figs. 4(b) and 4(c) is shown as (A − B) in Fig. 4(d). Quite surprisingly, the purely structural RPED pattern (A − B) is identical, up to a constant scaling factor of $R \equiv I_{\mathrm{MCD}}/I_{\mathrm{A-B}} = -0.84$, with the MCD pattern in Fig. 4(a). This may be explained by the fact that A − B (MCD) can be written as the sum (difference) of two purely structural patterns, which have the same angular distribution; see SM for details [24]. Also for the L_2 resonance [Figs. 4(f)–4(h)], the MCD pattern is exactly the same as (A − B), except for a constant factor $R = +0.61$.

These R values (−0.84, 0.61) are very close to the intensity ratio between the angle-integrated CD(A) and RPES in Fig. 2(d) at corresponding photon energies (639.7 and 651.8 eV), so we have

$$\frac{I_{\mathrm{MCD}}(\omega,\Omega)}{I_{\mathrm{A-B}}(\omega,\Omega)} = R(\omega) \approx \frac{I_{\mathrm{CD(A)}}(\omega)}{I_{\mathrm{RPES}}(\omega)} \approx \frac{I_{\mathrm{XMCD(A)}}(\omega)}{I_{\mathrm{XAS}}(\omega)}, \qquad (3)$$

where the function $R(\omega)$ is independent of the solid angle Ω and Eq. (1) has been used. Figure 4 and Eq. (3) show that the MCD signal, if normalized by the purely structural signal (A-B), approximately measures the XMCD of one sublattice. The quality of this approximation might depend on the material and deserves further investigation. Equation (3) suggests that MCD in RPED may be used in conjunction with the XMCD sum rules [9,10] for obtaining the sublattice magnetization in AMs directly from experiment. In practice, for obtaining the ratio $R(\omega)$ in Eq. (3) one can simulate the purely structural RPED patterns of sublattices (A) and (B) as in Fig. 4. Importantly, such a simulation is independent of the magnetic state and only requires structural information. Moreover, patterns (A) and (B) are related by a known symmetry operation (a rotation by π around z in the case of MnTe). The intensity of the sum $(\mathrm{A}+\mathrm{B})$ must be normalized to the experimentally measured signal $(\mathrm{A}+\mathrm{B}) = (\uparrow+) + (\uparrow-) + (\downarrow+) + (\downarrow-)$. Then, the ratio R is easily obtained as the best-fit proportionality factor between the measured MCD and the simulated $(\mathrm{A}-\mathrm{B})$ pattern.

We have defined the MCD in RPED as the difference between two CD patterns for opposite orientations of the Néel vector (CD↑ and CD↓) i.e., the CD patterns of two altermagnetic domains. Experimentally, it might be difficult to prepare samples for different magnetic domains. In this case, instead of CD↓, one can measure the CD of the demagnetized sample, which is the average of CD↑ and CD↓. The pattern CD↓ can then be recovered by subtraction. In a multidomain sample, the MCD signal is proportional to the average of $\cos\theta$, where θ is the angle between the local Néel vector $\mathbf{L}$ and the light helicity $\mathbf{q}$. This follows directly from the corresponding angular dependence of the XMCD of one sublattice. Therefore, MCD in RPED can in principle be used to map the distribution of the Néel vector [30].

In summary, we have presented a theory of RPED from altermagnets and applied it to MnTe at the Mn $L_{2,3}$-edge resonance. We find a large magnetic CD signal in the RPED pattern for parallel geometry, where the XMCD in absorption vanishes. We have shown that the occurrence of magnetic CD in RPED is a direct consequence of the XMCD on each magnetic sublattice and the fact that in an AM, the two sublattices necessarily have distinct PED patterns. Upon normalizing the MCD signal with the structural difference pattern of the two sublattices, it should be possible to extract the approximate XMCD spectrum of one AM sublattice and thus obtain the atomic magnetic moments directly from the experimental data. Our main findings are valid for any AM and lay the ground for making CD-RPED a powerful technique for the magnetic characterization of AM candidate materials.

Acknowledgments—I thank Alberto Marmodoro and the late Ondrej Šipr for bringing my attention to circular dichroism in altermagnets.

Data availability—The data that support the findings of this article are not publicly available upon publication because it is not technically feasible and/or the cost of preparing, depositing, and hosting the data would be prohibitive within the terms of this research project. The data are available from the authors upon reasonable request.

[1] S. Hayami, Y. Yanagi, and H. Kusunose, Momentum-dependent spin splitting by collinear antiferromagnetic ordering, J. Phys. Soc. Jpn. **88**, 123702 (2019).

[2] L. Šmejkal, R. González-Hernández, T. Jungwirth, and J. Sinova, Crystal time-reversal symmetry breaking and spontaneous Hall effect in collinear antiferromagnets, Sci. Adv. **6**, eaaz8809 (2020).

[3] L. Šmejkal, J. Sinova, and T. Jungwirth, Emerging research landscape of altermagnetism, Phys. Rev. X **12**, 040501 (2022).

[4] C.-T. Chou, S. Ghosh, B. C. McGoldrick, T. Nguyen, G. Gurung, E. Y. Tsymbal, M. Li, K. A. Mkhoyan, and L. Liu, Large spin polarization from symmetry-breaking antiferromagnets in antiferromagnetic tunnel junctions, Nat. Commun. **15**, 7840 (2024).

[5] T. Jungwirth, X. Marti, P. Wadley, and J. Wunderlich, Antiferromagnetic spintronics, Nat. Nanotechnol. **11**, 231 (2016).

[6] L. Han, X. Fu, R. Peng, X. Cheng, J. Dai, L. Liu, Y. Li, Y. Zhang, W. Zhu, H. Bai, Y. Zhou, S. Liang, C. Chen, Q. Wang, X. Chen, L. Yang, Y. Zhang, C. Song, J. Liu, and F. Pan, Electrical 180° switching of Néel vector in spin-splitting antiferromagnet, Sci. Adv. **10**, eadn0479 (2024).

[7] J. Krempaský *et al.*, Altermagnetic lifting of Kramers spin degeneracy, Nature (London) **626**, 517 (2024).

[8] P. Keßler, L. Garcia-Gassull, A. Suter, T. Prokscha, Z. Salman, D. Khalyavin, P. Manuel, F. Orlandi, I. I. Mazin, R. Valentí, and S. Moser, Absence of magnetic order in RuO2: Insights from μsr spectroscopy and neutron diffraction, npj Spintron. **2**, 50 (2024).

[9] B. T. Thole, P. Carra, F. Sette, and G. van der Laan, X-ray circular dichroism as a probe of orbital magnetization, Phys. Rev. Lett. **68**, 1943 (1992).

[10] P. Carra, B. T. Thole, M. Altarelli, and X. Wang, X-ray circular dichroism and local magnetic fields, Phys. Rev. Lett. **70**, 694 (1993).

[11] A. Hariki, A. Dal Din, O. J. Amin, T. Yamaguchi, A. Badura, D. Kriegner, K. W. Edmonds, R. P. Campion, P. Wadley, D. Backes, L. S. I. Veiga, S. S. Dhesi, G. Springholz, L. Šmejkal, K. Výborný, T. Jungwirth, and J. Kuneš, X-ray magnetic circular dichroism in altermagnetic α-MnTe, Phys. Rev. Lett. **132**, 176701 (2024).

[12] N. Sasabe, M. Mizumaki, T. Uozumi, and Y. Yamasaki, Ferroic order for anisotropic magnetic dipole term in collinear antiferromagnets of $(t_{2g})^4$ system, Phys. Rev. Lett. **131**, 216501 (2023).

[13] A. Hariki, Y. Takahashi, and J. Kuneš, X-ray magnetic circular dichroism in $\mathrm{RuO_2}$, Phys. Rev. B **109**, 094413 (2024).

[14] A. Hariki, K. Sakurai, T. Okauchi, and J. Kuneš, Separating altermagnetic and ferromagnetic effects in x-ray magnetic dichroism of rutile NiF2, npj Quantum Mater. **10**, 49 (2025).

[15] C. S. Fadley, Angle-resolved x-ray photoelectron spectroscopy, Prog. Surf. Sci. **16**, 275 (1984).

[16] P. Krüger, S. Bourgeois, B. Domenichini, H. Magnan, D. Chandesris, P. Le Fèvre, A. M. Flank, J. Jupille, L. Floreano, A. Cossaro, A. Verdini, and A. Morgante, Defect states at the TiO_2(110) surface probed by resonant photoelectron diffraction, Phys. Rev. Lett. **100**, 055501 (2008).

[17] M. Morscher, F. Nolting, T. Brugger, and T. Greber, Resonant photoelectron diffraction with circularly polarized light, Phys. Rev. B **84**, 140406(R) (2011).

[18] R. Sagehashi, G. Park, and P. Krüger, Theory of circular dichroism in angle-resolved resonant photoemission from magnetic surfaces, Phys. Rev. B **107**, 075407 (2023).

[19] F. Matsui, M. Fujita, T. Ohta, N. Maejima, H. Matsui, H. Nishikawa, T. Matsushita, and H. Daimon, Selective detection of angular-momentum-polarized auger electrons by atomic stereography, Phys. Rev. Lett. **114**, 015501 (2015).

[20] H. Daimon, T. Nakatani, S. Imada, S. Suga, Y. Kagoshima, and T. Miyahara, Strong circular dichroism in photoelectron diffraction from nonchiral, nonmagnetic material–direct observation of rotational motion of electrons, Jpn. J. Appl. Phys. **32**, L1480 (1993).

[21] B. Sinkovic, L. H. Tjeng, N. B. Brookes, J. B. Goedkoop, R. Hesper, E. Pellegrin, F. M. F. de Groot, S. Altieri, S. L. Hulbert, E. Shekel, and G. A. Sawatzky, Local electronic and magnetic structure of Ni below and above T_c: A spin-resolved circularly polarized resonant photoemission study, Phys. Rev. Lett. **79**, 3510 (1997).

[22] G. van der Laan, Comment on "local electronic and magnetic structure of Ni below and above T_c: A spin-resolved circularly polarized resonant photoemission study," Phys. Rev. Lett. **81**, 733 (1998).

[23] F. Da Pieve and P. Krüger, First-principles calculations of angle-resolved and spin-resolved photoemission spectra of Cr(110) surfaces at the $2p-3d$ Cr resonance, Phys. Rev. Lett. **110**, 127401 (2013).

[24] See Supplemental Material at http://link.aps.org/supplemental/10.1103/pl1p-v5rs for computational details, fundamental RPED patterns, an explanation why the pattern MCD is proportional to (A − B), and bulk calculations for MnTe and MnO, which includes Refs. [25–27].

[25] A. Tanaka and T. Jo, Resonant 3d, 3p and 3s photoemission in transition metal oxides predicted at 2p threshold, J. Phys. Soc. Jpn. **63**, 2788 (1994).

[26] M. P. Seah and W. A. Dench, Quantitative electron spectroscopy of surfaces: A standard data base for electron inelastic mean free paths in solids, Surf. Interface Anal. **1**, 2 (1979).

[27] W. L. Roth, Magnetic structures of MnO, FeO, CoO, and NiO, Phys. Rev. **110**, 1333 (1958).

[28] P. Krüger, *Ab initio* calculation of ligand field multiplet parameters for transition metal l-edge spectra, Radiat. Phys. Chem. **175**, 108051 (2020).

[29] F. J. García de Abajo, M. A. Van Hove, and C. S. Fadley, Multiple scattering of electrons in solids and molecules: A cluster-model approach, Phys. Rev. B **63**, 075404 (2001).

[30] O. J. Amin *et al.*, Nanoscale imaging and control of altermagnetism in MnTe, Nature (London) **636**, 348 (2024).

Supplemental Material for
Circular dichroism in resonant photoelectron diffraction as a direct probe of sublattice magnetization in altermagnets

Peter Krüger
Graduate School of Engineering and Molecular Chirality Research Center, Chiba University, Chiba 263-8522 Japan

The following supplementary information is given. (i) Computational details. (ii) Fundamental RPED patterns are defined and shown for L_2- and L_3-resonance with Néel vector along x or z. (iii) An explanation is given why the magnetic CD pattern is, up to a constant factor, identical with the structural pattern (A−B). (iv) RPED calculations for bulk MnTe are shown, which demonstrates that the magnetic CD in RPED is not a surface effect. (v) Comparison with a conventional antiferromagnet (MnO).

(i) Computational details

The numerical calculations have been done with our recent method for RPED [1] which combines crystal field multiplet theory [2] for the resonant photoemission process and multiple scattering theory for the propagation of the photoelectron wave [3, 4]. The resonant photoemission amplitude of the emitter atoms are computed in a ligand field multiplet model using second order perturbation theory (Kramers-Heisenberg formula) [3, 4]. The Mn-2p and 3d level energies are adapted from experiment. The atomic Coulomb and spin-orbit integrals are taken from Tanaka and Jo [5] for a Mn^{2+} ion and the crystal field is taken from A. Hariki et al. [6]. In order to orient the local magnetic moment to the experimentally observed $[1\bar{1}00]$ direction, a small exchange field of 1 meV is applied. The $2p$ core-hole lifetime is set to $\Gamma = 0.4$ eV [6]. The same multiplet model is used to compute the X-ray absorption and XMCD spectra (Fig. 2a,b in the main text) and the results agree very well with A. Hariki et al. [6].

For computing the RPED pattern, i.e. the angular distribution of the resonant photoemission intensity, a photoelectron diffraction (PED) calculation is performed with the EDAC code [4] for each multiplet final state and the RPED intensities are summed. For a Mn^{2+} ion, there are 210 final states in the $(3d^4)$ configuration. The source waves of these PED calculations are constructed from the resonant photoemission amplitudes obtained in the multiplet calculation, see Ref. [1] for details. In the PED calculation the inelastic mean free path is set to 1.37 nm, according to the universal curve [7]. The multiple scattering series is truncated at 5th order, which is found sufficient for convergence of the RPED patterns. The MnTe surface is modeled with finite clusters of 479 atoms of semi-ellipsoid shape, see Fig. 1b in the main text. The clusters have a diameter and depth of 2.7 nm, which is twice the inelastic mean free path. Two surface terminations, Te/Mn-A and Te/Mn-B, are considered and the results are averaged.

(ii) Fundamental RPED patterns

In RPED from an AM with Néel vector **L** and circular polarized light of helicity **q**, there are four possible parallel alignments between **L** (↑,↓) and **q** (±), namely (↑+), (↑−), (↓+) and (↓−). We define the four "fundamental" linear combinations as

$$
\begin{aligned}
\mathrm{SPD} &= (\uparrow +) + (\uparrow -) + (\downarrow +) + (\downarrow -)\\
\mathrm{SCD} &= (\uparrow +) - (\uparrow -) + (\downarrow +) - (\downarrow -)\\
\mathrm{MPD} &= (\uparrow +) + (\uparrow -) - (\downarrow +) - (\downarrow -)\\
\mathrm{MCD} &= (\uparrow +) - (\uparrow -) - (\downarrow +) + (\downarrow -)
\end{aligned}
$$

where SPD, SCD, MPD and MCD stand for structural RPED, structural CD, magnetic RPED and magnetic CD, respectively. These patterns are shown in Fig. S1 for the Mn L_3-edge or L_2-edge with **L**, **q** along $x = [1\bar{1}00]$ or $z = [0001]$.

In the SPD pattern, **L** and **q** are averaged over opposite signs, so SPD corresponds to a demagnetized sample with random AM domains and non-polarized light, and it contains no magnetic information. Accordingly, the patterns have the 6-fold symmetry of the (stepped) MnTe(0001) surface. The SCD pattern reflects the common CD in angular distribution in photoemission, which for X-ray PED is also known as the Daimon effect. The MPD pattern corresponds to the RPED contrast between two AM domains with opposite **L** when using unpolarized light. The fact that this signal is non-zero in Fig. S1, directly shows that RPED is sensitive to the sublattice magnetization in AMs. The MCD pattern is the purely magnetic CD and has been discussed in some detail in the main text.

In Fig. S1, the fundamental patterns are shown for the L_2 and the L_3-resonance with **L** and **q** along the x or z-axis. Looking at $L_2(x)$ and $L_3(x)$ in Figs S1 (a,b) we see that the SPD pattern has the 6-fold symmetry of the macroscopic surface. Since SPD is a symmetric combination of $\mathbf{L} = \uparrow, \downarrow$ and $\mathbf{q} = \pm$, the orientation of **L** and **q** along x does not break the symmetry. The pattern MCD has only 3-fold symmetry and it changes sign under 2-fold rotation around z, which reflects the point symmetry of

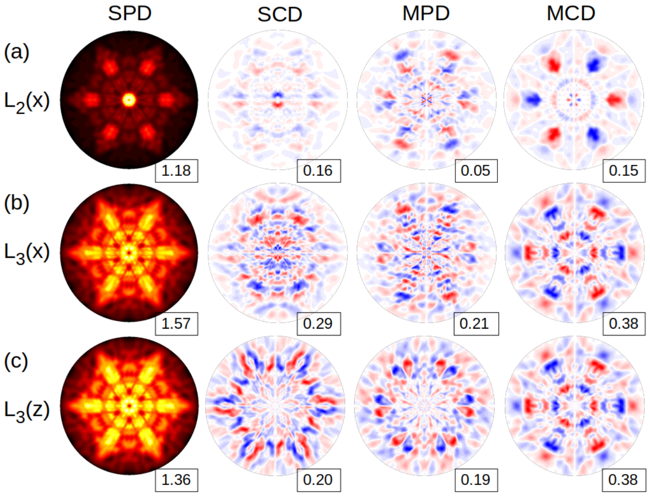

FIG. S1. Calculated RPED patterns of MnTe(0001) with circular polarized light in parallel geometry. (a) L_2-resonance ($\hbar\omega$=651.8eV). $\mathbf{L}$, $\mathbf{q} \sim x$. (b) L_3-resonance ($\hbar\omega$=639.7eV). $\mathbf{L}$, $\mathbf{q} \sim x$. (c) L_3-resonance. $\mathbf{L}$, $\mathbf{q} \sim z$. The columns show the four fundamental patterns as defined in section (i). The color scale is always from minimum to maximum intensity, which is indicated in the small boxes. In SPD, the minimum is black and the maximum is yellow. In the other patterns, red is positive, blue is negative and white is zero.

the individual Mn sites (S_6). In the SCD pattern, the 3-fold symmetry is broken by the helicity vector along x. The Daimon effect is well seen, especially at the Mn-Mn forward focussing peak at the center of pattern L_2(x)-SCD. In the MPD pattern the 3-fold symmetry is broken by the Néel vector along x.

Comparing the patterns for $L_2(x)$ and $L_3(x)$, the peak intensities are quite different, which indicates that the angular distribution of source wave depends strongly on magnetic moment of the core-hole ($j = 1/2$ or $j = 1/2$). However the peak positions are rather similar, as they appear in both cases at forward focussing directions, see Fig. 1(c) of the main text.

When comparing the patterns $L_3(x)$ and $L_3(z)$ in Figs. S1(b,c), we see that the SPD patterns are very similar. The small difference is due to the fact that “unpolarized” light is actually polarized in the plane perpendicular to $\mathbf{q}$. In contrast, the patterns SCD and MPD are very different between $L_3(x)$ and $L_3(z)$, i.e. they depend strongly on the orientation of $\mathbf{L}, \mathbf{q}$ relative to the crystal axes.

Surprisingly, the MCD patterns for $L_3(x)$ and $L_3(z)$ are *exactly* identical. So the MCD signal depends only on the relative orientation between the Néel vector and the light helicity, rather than on the orientation of these vectors w.r.t. the crystal axes. This is a remarkable finding because the axes $[1\bar{1}00]$ and $[0001]$ are not symmetry related. It shows that the MCD pattern is free of structural CD effects and thus really measures the magnetic properties.

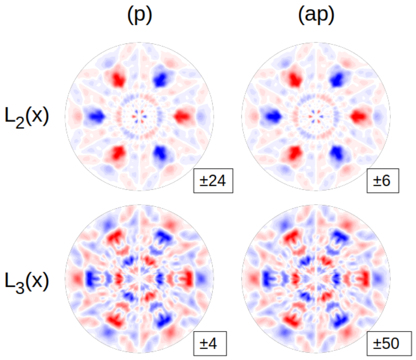

FIG. S2. RPED patterns (p) and (ap) as defined in section (ii) for MnTe(0001) with circular polarized light at the L_2 or L_3-resonance with $\mathbf{L}$, $\mathbf{q} \sim x$. For each pattern, the maximum intensity is indicated in the small box. The normalization is the same as in Fig.4 of the main text.

(iii) Why is the magnetic CD proportional to the structural pattern (A−B)?

As seen in Fig. 4 of the main text, the MCD pattern is, up to a constant intensity scaling, identical with the purely structural pattern (A−B). Here we give an explanation for this important result. To this end, we decompose the pattern (A−B) into two contributions, with either parallel (p) or antiparallel (ap) alignment between the local spins and the helicity vector. These patterns are defined as follows.

$$(p) = (a{\uparrow}+) + (a{\downarrow}-) - (b{\uparrow}+) - (b{\downarrow}-)$$
$$(ap) = (a{\uparrow}-) + (a{\downarrow}+) - (b{\uparrow}-) - (b{\downarrow}+)$$

where $(a{\uparrow}+)$ is the RPED signal due to emission from sites A only, with *local* spin orientation ↑ and light helicity +. Similarly $(b{\downarrow}-)$ corresponds to emission from site B with spin ↓ and helicity −. Note that Néel vector $\mathbf{L} = \uparrow$ corresponds to $(a\uparrow)$ and $(b\downarrow)$. The signals (p) and (ap) are structural RPED patterns which measure a contrast between emission from sites A and B. They are invariant under reversal of either Néel vector or helicity (or both). They have the same symmetry and are not directly related to the magnetic state ($\mathbf{L}$) of the system or the light polarization ($\mathbf{q}$). Therefore we expect them to have the same angular distribution due to photoelectron diffraction. The calculated patterns (p) and (ap) are shown in Fig. S2 for the L_2 and L_3 resonances with $\mathbf{L}$ and $\mathbf{q} \sim x$. (p) and (ap) are indeed identical except for the overall intensity (indicated in the boxes). We have

$$(\text{A}-\text{B}) = (p) + (ap) \ ,$$

so (A−B) has the same symmetry and the same angular distribution as (p) and (ap). The difference between (p) and (ap) is the relative alignment between local spin and light helicity, which is parallel in (p) and antiparallel in (ap). This changes the local XMCD effect and

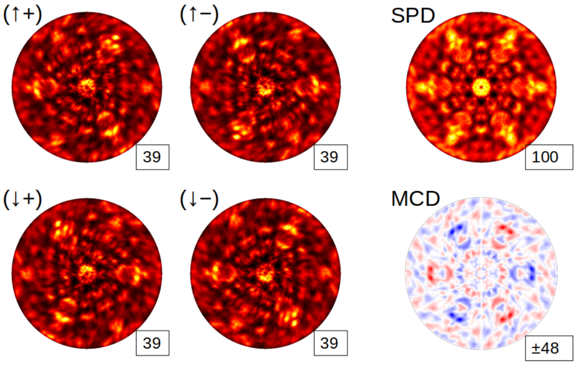

FIG. S3. RPED patterns for bulk MnTe with circular polarized light at the L_3-resonance ($\hbar\omega = 639.7$ eV) with $\mathbf{L}$, $\mathbf{q} \sim x$. For each pattern, the maximum intensity is indicated in the small box relative to the SPD pattern, whose maximum is put to 100.

so the difference between (p) and (ap) is related to the XMCD contrast between sublattices A and B. From the definitions it is easy to see that

$$\mathrm{MCD} = (p) - (ap)\ .$$

Since patterns (p) and (ap) have the same angular dependence, their sum (A−B) and difference (MCD) also have this same angular dependence, which is indeed the case, see Fig. 4 in the main text.

So the reason why the patterns (A−B) and MCD are identical, up to a constant scaling factor, is that they are the sum and difference, respectively, of two patterns (p) and (ap) with the same angular dependence. (p) and (ap) have the same angular dependence because they are purely structural RPED signals with the same symmetry. They differ only in the relative alignment between $\mathbf{L}$ and $\mathbf{q}$, which determines the overall intensity through the local XMCD effect.

(iv) RPED calculations for bulk MnTe.

In order to prove that the appearance of the MCD signal is not a surface effect, we have performed RPED calculations for bulk MnTe using spherical clusters of 447 atoms with a single Mn emitter site at the center. Calculations were done for two clusters, for emission from Mn-A and Mn-B, and the intensities were summed. Fig. S3 shows the results for the L_3-resonance ($\hbar\omega$=639.7eV) with $\mathbf{L}$, $\mathbf{q} \sim x$. The individual patterns $(\uparrow +)$, $(\uparrow -)$, $(\downarrow +)$, $(\downarrow -)$ are shown, along with the combinations SPD and MCD, defined in section (i).

The patterns are different from those of the MnTe(0001) surface calculation in Figs.3,4(a),S1(b). The bulk patterns in Fig. S3 display more fine structure and sharper diffraction peaks, which is expected because photoelectrons emitted from a bulk site experience more scattering events. Importantly however, the symmetry of all patterns is the same for bulk and surface, and the positions of the dominant peaks is similar. The amplitude of the MCD signal is comparable with that of the surface, considering the more homogeneous intensity distribution of the latter. These results clearly show that the magnetic CD in RPED of altermagnets is not a surface effect but essentially a bulk property.

(v) Comparison with a conventional antiferromagnet (MnO)

Here we present RPED calculations for the conventional antiferromagnet MnO. MnO has rocksalt structure and an antiferromagnetic order with ferromagnetically aligned (111) planes whose spin direction alternates along [111]. The sublattice magnetization is in-plane [8], but for simplicity we take the Néel vector $\mathbf{L}$ out-of-plane along the [111] axis, see Fig. S4a. As in section (iv) the calculation is done for an oriented crystal in the bulk. We used a spherical cluster of 389 atoms with a single Mn emitter at the center. Fig. S4 b shows the calculated RPED patterns at the maximum of the Mn L_3-resonance ($\hbar\omega = 639.7$ eV) in parallel geometry, i.e. with $\mathbf{L}$, $\mathbf{q} \sim z$. $(+)$ and $(-)$ denote right and left circular polarization. SPD is the sum of $(+)$ and $(-)$ and SCD is the difference. Fig. S4 b gives the contributions from the two sublattices A and B. (Note that these single-sublattice contributions are not measurable.)

All the patterns have three main peaks which correspond to the Mn→O nearest-neighbor forward focussing directions. This is similar to the main PED peaks from Mn-A sites in MnTe, which are caused by Mn-A→Te focussing (see Fig. 1c of the main text). Indeed, with the chosen crystal orientations, the Mn-A sites in MnTe and *all* Mn sites in MnO have an octahedral environment with the same orientation. The crucial difference between the altermagnet MnTe and the conventional antiferromagnet MnO is that in MnO, all octahedra have the same orientation, while in MnTe, the octahedra of the Mn-B sites are rotated by π around z, giving a totally different PED pattern (Fig. 1c and Fig. 4b,c in the main text).

The RPED patterns of MnO in Fig. S4 c all look very similar, but the total intensity (indicated in the small boxes) depends strongly on relative alignment between local magnetic moment $\mathbf{m}$ and the light helicity $\mathbf{q}$. For A(+) and B(−) the alignment is parallel ($\mathbf{m} \cdot \mathbf{q} > 0$) and the intensity is weak. For A(−) and B(+) with antiparallel alignment, the intensity is almost 10 times larger. As already explained for MnTe in the main text, the reason for this strong intensity difference is the large negative XMCD effect at the Mn L_3-edge, where X-ray absorption (and thus also resonant photoemission) is maximum when $\mathbf{m}$ and $\mathbf{q}$ are antiparallel.

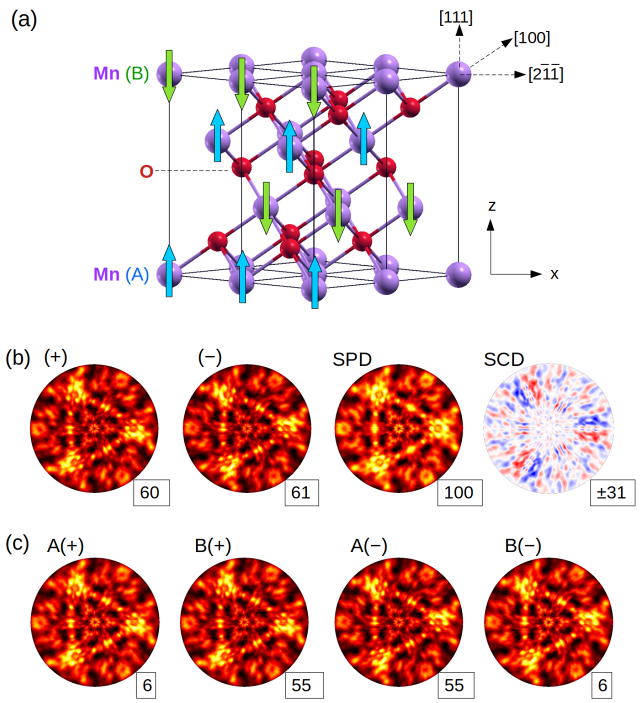

FIG. S4. (a) Ball-and-stick model of bulk MnO with the [111] axis oriented along z. The antiferromagnetic ground state with ferromagnetically aligned (111) layers is shown. The Néel vector is taken $\mathbf{L} \sim z$. Mn(A) and Mn(B) denote the spin-up and spin-down sublattice, respectively. (b) RPED patterns for bulk MnO with circular polarized light at the maximum of the Mn L$_3$-resonance ($\hbar\omega = 639.7$ eV) with $\mathbf{L}$, $\mathbf{q} \sim [111] = z$. (+) and (−) correspond to right and left circular polarized light. SPD is the sum and SCD is the difference of (+) and (−). For each pattern, the maximum intensity is indicated in the small box relative to the SPD pattern, whose maximum is put to 100. (c) Decomposition of the patterns (+) and (−) into their contributions from sites A and B.

The structural CD (pattern SCD) is large with ±31%. The MCD signal (not shown) is exactly zero. This can be understood as follows. Upon time-reversal, i.e. when the Néel vector $\mathbf{L}$ and thus all the Mn spins are reversed, the RPED patterns of sublattices A and B are interchanged, e.g. pattern A(+) becomes B(+). This does not change any experimentally measurable pattern, where the signals from the two sublattices are summed. Therefore, time-reversal does not change any (experimentally measurable) RPED pattern. As a consequence, the magnetic CD, defined as MCD=CD($\mathbf{L}$)−CD($-\mathbf{L}$) is exactly zero. For the same reason, the MPD signal is also exactly zero.

In a compensated magnetic structure, time-reversal is equivalent to interchanging the two magnetic sublattices A and B. In a conventional antiferromagnet, this transformation is a translation by a Bravais lattice vector and does not change the crystal orientation. As a consequence, the RPED patterns of two sublattices A and B are simply swapped (rather than rotated as in an altermagnet). Then, any experimental RPED signal (which is the sum of A and B) is time-reversal even. It follows that the magnetic signals MCD and MPD, which are time-reversal odd by definition, must vanish exactly.

[1] R. Sagehashi, G. Park, and P. Krüger, Theory of circular dichroism in angle-resolved resonant photoemission from magnetic surfaces, Phys. Rev. B **107**, 075407 (2023).
[2] P. Krüger, Ab initio calculation of ligand field multiplet parameters for transition metal l-edge spectra, Radiation Physics and Chemistry **175**, 108051 (2020).
[3] C. S. Fadley, Angle-resolved x-ray photoelectron spectroscopy, Progress in Surface Science **16**, 275 (1984).
[4] F. J. García de Abajo, M. A. Van Hove, and C. S. Fadley, Multiple scattering of electrons in solids and molecules: A cluster-model approach, Phys. Rev. B **63**, 075404 (2001).
[5] A. Tanaka and T. Jo, Resonant 3d, 3p and 3s photoemission in transition metal oxides predicted at 2p threshold, Journal of the Physical Society of Japan **63**, 2788 (1994).
[6] A. Hariki, A. Dal Din, O. J. Amin, T. Yamaguchi, A. Badura, D. Kriegner, K. W. Edmonds, R. P. Campion, P. Wadley, D. Backes, L. S. I. Veiga, S. S. Dhesi, G. Springholz, L. Šmejkal, K. Výborný, T. Jungwirth, and J. Kuneš, X-ray magnetic circular dichroism in altermagnetic α-mnte, Phys. Rev. Lett. **132**, 176701 (2024).
[7] M. P. Seah and W. A. Dench, Quantitative electron spectroscopy of surfaces: A standard data base for electron inelastic mean free paths in solids, Surface and Interface Analysis **1**, 2 (1979).
[8] W. L. Roth, Magnetic structures of mno, feo, coo, and nio, Phys. Rev. **110**, 1333 (1958).